LA-UR-15-27372
Approved for public release; distribution is unlimited.

Title: Characterization of Tubing from Advanced ODS alloy (FCRD-NFA1)

Author(s): Maloy, Stuart Andrew
Aydogan, Eda
Anderoglu, Osman
Lavender, Curt
Anderson, Iver
Rieken, Joel
Lewandowski, John
Hoelzer, Dave
Odette, George R.

Intended for: Report

Issued: 2016-09-20 (rev.1)

# *Characterization of Tubing from Advanced ODS alloy (FCRD-NFA1)*

## Fuel Cycle Research & Development

***Prepared for***
***U.S. Department of Energy***
***Advanced Fuels Campaign***

***Stuart A. Maloy, Eda Aydogan, O. Anderoglu, Los Alamos National Laboratory***
***Curt Lavender, Pacific Northwest National Laboratory***
***Iver Anderson, Joel Rieken, Ames Laboratory***
***John Lewandowski, Case Western Reserve University***
***Dave Hoelzer, Oak Ridge National Laboratory***
***George R. Odette, UC Santa Barbara***
***LA-UR-***

THIS PAGE INTENTIONALLY LEFT BLANK

# SUMMARY

Fabrication methods are being developed and tested for producing fuel clad tubing of the advanced ODS 14YWT and FCRD-NFA1 ferritic alloys. Three fabrication methods were based on plastically deforming a machined thick wall tube sample of the ODS alloys by pilgering, hydrostatic extrusion or drawing to decrease the outer diameter and wall thickness and increase the length of the final tube. The fourth fabrication method consisted of the additive manufacturing approach involving solid-state spray deposition (SSSD) of ball milled and annealed powder of 14YWT for producing thin wall tubes. The details of these fabrication methods are described in ORNL/TM-2015/499 "Status of producing 5 inch long clad tubing of ODS ferritic alloys." Of the four fabrication methods, two methods were successful at producing tubing for further characterization: production of tubing by High velocity oxy-fuel spray forming and production of tubing using high temperature hydrostatic extrusion. The characterization described in the following report shows through neutron diffraction the texture produced during extrusion while maintaining the beneficial oxide dispersion. Future work will center on extending these processes to producing longer tubing for characterization and irradiation testing.

THIS PAGE INTENTIONALLY LEFT BLANK

# CONTENTS

# ACRONYMS

| | |
|---|---|
| BCC | Body Centered Cubic |
| EBSD | Electron Backscatter Detection |
| ED | Extrusion Direction |
| HAB | High Angle Boundary |
| HIP | Hot Isostatic Pressing |
| HIPPO | High Pressure/Preferred Orientation Instrument |
| LAB | Low Angle Boundary |
| ND | Normal to the rolling direction |
| NF | NanoFeatures |
| NFA | Nanostructured Ferritic Alloys |
| ODF | Orientational Distribution Function |
| ODS | Oxide Dispersion Strengthened |
| OIM | Orientational Imaging Microscope |
| ORNL | Oak Ridge National Laboratory |
| RD | Rolling Direction |
| SEM | Scanning Electron Microscope |
| TD | Transverse to the rolling direction |
| TOF | Time of Flight |
| UCSB | University of California Santa Barbara |

**Abstract:**
In this research, the parameters for innovative thermal spray deposition and hot extrusion processing methods have been developed to produce the final nanostructured ferritic alloy (NFA) tubes having approximately 0.5 mm wall thickness. Effect of different processing routes on texture and grain boundary characteristics has been investigated. It was found that hydrostatic extrusion results in combination of plane strain and shear deformations which generate rolling textures of α- and γ-fibers on {001}<110> and {111}<110> together with a shear texture of ζ-fiber on {011}<211> and {011}<011>. On the other hand, multi-step plane strain deformation in cross directions leads to a strong rolling textures of θ- and ε-fiber on {001}<110> together with weak γ-fiber on {111}<112>. Even though the amount of the equivalent strain is similar, shear deformation leads to much lower texture indexes compared to the plane strain deformations. Moreover, while 50% of hot rolling brings about a large number of high angle grain boundaries (HAB), 44% of shear deformation results in large amount of low angle boundaries (LAB) showing the incomplete recrystallization.

**Introduction:**
Nanostructured ferritic alloys are considered to be one of the best candidates for structural components in nuclear reactors due to their irradiation resistance, high strength, resistance to oxidation/corrosion under extreme conditions of temperature and pressure [1–6]. Recently, nanostructured alloys having uniform microstructure with 1-2 nm Ti-Y-O rich nanofeatures (NFs) have been developed by Oak Ridge National Laboratory (ORNL) and University of California Santa Barbara (UCSB) [7]. Those very small NFs provide higher strength and better thermal stability to NFAs. Moreover, they serve as sink for He gas and trap it in extremely small bubbles during neutron irradiation, resulting in a reduction in void swelling [8-12]. At present, there are a number of studies for NFA production and processing, alloys still being developed and improved; therefore understanding of their microstructure and anisotropy during fabrication is crucial [13]. Ukai and Fujiwara studied numerous processing methods and parameters in order to understand microstructure and anisotropy [14]. It is suggested that improved high temperature properties can be obtained by using the consolidation methods of hot extrusion (HE), hot rolling or hot isostatic pressing (HIP) combined with hot forging after mechanical alloying (MA) of powders. Recently, Hoelzer et al. [15] achieved sub-micrometer grain size and homogeneous microstructure on a 14%Cr nanostructured ferritic alloys (14YWT) by using a processing method consisting of hot extrusion and multistep hot rolling. Consequently, 14YWT steels with outstanding mechanical properties such as high temperature tensile and creep strength up to 800˚C were manufactured. Still, these 14YWT alloys exhibit poor ductility and fracture toughness [16,17]**.** On the other hand, recent studies suggest that hydrostatic extrusion can generate not only notably isotropic and enhanced mechanical properties but also high density of consolidation [18–20]. Lewandowski et al. [21] reported that hydrostatic pressure can change the flow stress state and increase the ductility of NiAl intermetallics having BCC crystal structure. The changes in the flow properties were attributed to both the increase in the mobile dislocation density through the pressure-induced punching of dislocations from elastically anisotropic interfaces in the microstructures [22,23] and the breakaway of dislocations from interstitial atmospheres pinning them [24].
Gaining an understanding of the resulting microstructure in terms of crystallographic texture (distribution of grain orientations) and grain boundary characteristics is critical since microstructure determines most of the bulk materials properties. Ferritic steels having BCC structure generally develop fiber-type textures during deformation and annealing [25]. The most common fiber textures are α-fiber consisting of orientations with <110> direction parallel to rolling direction (RD) (represented as <110>∥RD) and γ-fiber which is composed of {111}<hkl>

orientations, where {111} planes lie in the rolling plane (represented as <111>∥ND). Other less common fiber textures are ε-fiber (<011>∥TD), η-fiber (<100>∥RD), θ-fiber (<001>∥ND), and ζ-fiber (<011>∥ND) [26,27]. It has been reported that the fiber types and grain orientations control the formability of BCC materials [28-31]. Similarly, grain boundary misorientation determines the stored energy of deformation that is considered to be the driving force for primary recrystallization [32-35]. Moreover, plastic deformation leads to the formation of new boundary structures which consist of piled-up dislocations and divide the original grains into different orientations. Dislocation pile-ups and subdivision of the large grains into smaller structures are two hardening sources. In other words, increasing strain levels leads to an increase in misorientation between substructures which in turn increases the hardness of the materials [36].

In this study, we have investigated the effect of processing routes on the texture and grain boundary characteristics of 14YWT NFA tubes. Texture and grain boundary characteristics were analysed by neutron and electron diffraction methods.

**Experimental Procedure:**

In order to understand the effect of processing methods on the texture and boundary characteristics, 14YWT tubes were produced by two different routes. Process I is a novel method of thermal spraying and Process II is a conventional mechanical alloying method followed by hot extrusion. As described in Figure 1, Process I is the combination of gas atomization reaction synthesis (GARS) of Fe-based NFA precursor powders, deposited by high velocity oxy-fuel (HVOF) thermal spray methods on tubular pre-forms, followed by hot hydrostatic extrusion to final tubing dimensions. A “mother tube” was manufactured through HVOF deposition on an Al mandrel with L2307 Fe-based NFA precursor powders (20-53μm dia.). The fugitive Al mandrel was removed from the deposit section with a phosphoric acid etching treatment and initial machining was performed to remove the interior (~250μm) layer of intermetallic phase (FeAl or $Fe_3Al$) that appeared to form during the deposition process. The samples were then heat treated at 1000°C for 5hr under vacuum following thermal spray deposition to promote the oxygen exchange reaction and Y-Ti-O dispersoid formation within the coating. Finally, hot extrusion was applied two times to 4:1 area reduction (44% of equivalent strain) by using a solid support mandrel to assist a uniform deformation.

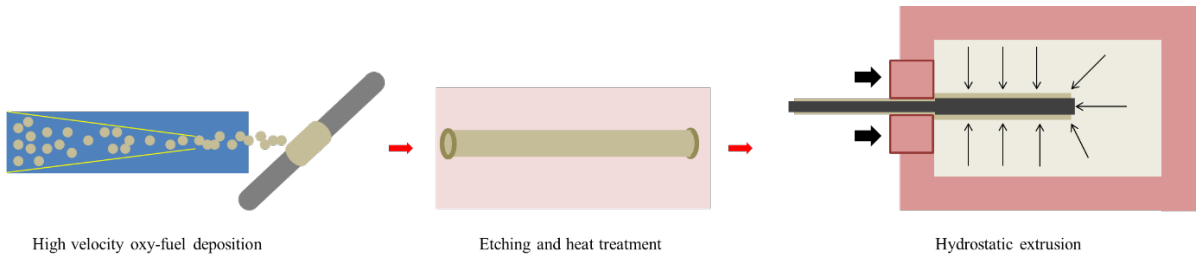


Figure 1: Processing steps of Process I

For Process II described in Figure 2, powders were produced by gas atomization method by ATI Powder Metals Laboratory (Pittsburgh, PA). After atomization the Y is phase separated and requires ball milling. A total of 15 kg of nominal 14wt%Cr-3wt%W-0.35wt%Ti-0.25wt%Y iron alloy powder was ball milled by Zoz, GmbH (Wenden, Germany) with 52.5 g of FeO powder for 40 h in a CM100b attritor mill with a ball mass-to-charge ratio of 10:1 and ball size of 5 mm. The canister was evacuated and backfilled with Ar three times to remove any atmosphere contamination and milled in Ar at an overpressure of 100 mbar. The milling speed alternated between 256 (2 minutes) and 150 rpm (10 minutes). FeO was added to increase the O content to~

0.08 wt.%. The powders were first canned and degassed at 400 ºC then hot extruded at 850 ºC. After extrusion the alloy was annealed for 1 h at 1000 ºC and hot cross-rolled to a~ 50% of equivalent strain resulting in the thickness of~ 10 mm. After boring with electro-discharge machining in the perpendicular direction of hot cross-rolling to get a tube shape, it was hydrostatically extruded to 4:1 area reduction at 815 °C.

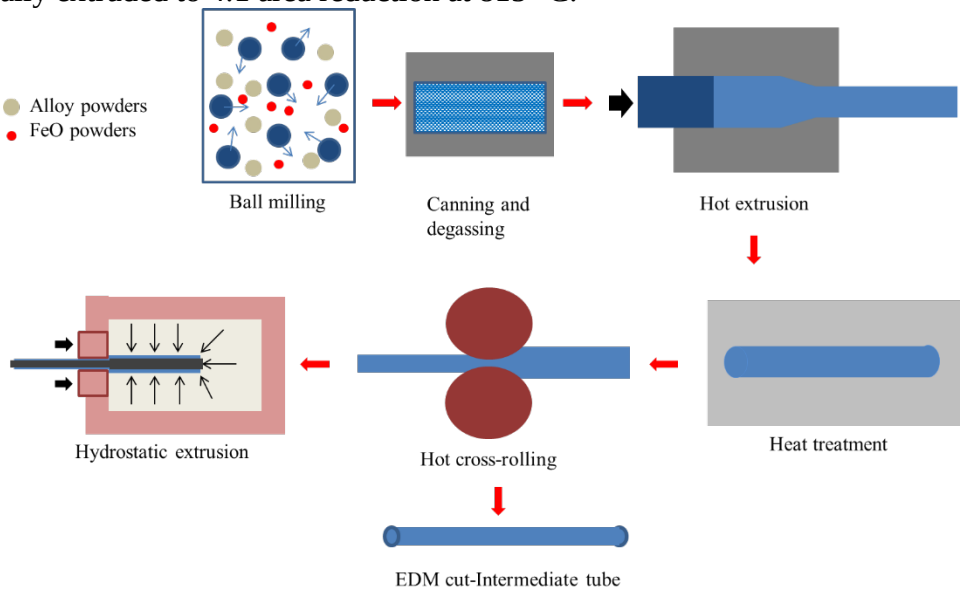


Figure 2: Processing steps of Process II

Figure 3 shows the final dimensions of the tubes. Final wall thickness of both of the tubes is~0.5 mm and outer diameters of tubes are~ 8 mm and 3.5 mm produced by Process I and Process II, respectively.

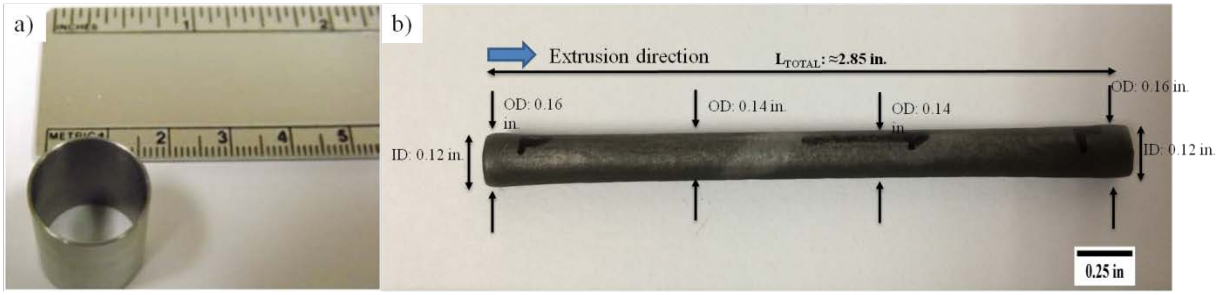


Figure 3: Photos showing the final dimension of the tubes produced by a) Process I and b) Process II.

Grain boundary characteristics were investigated by orientation imaging microscopy (OIM) while texture analysis was implemented using both OIM and neutron diffraction methods.

OIM has been used as a useful technique to study local texture, interface characteristics and their distribution as well as dislocation distribution. Resolution of OIM using a scanning electron microscope is limited to mesoscale studies of grain sizes down to 60 nm [37,38]. Electron backscatter diffraction (EBSD) is an OIM method that was used to examine the grain boundary characteristics and texture of NFAs. It is employed by using an FEI Inspect FEG SEM equipped with TSL EBSD equipment. Since the sample is tilted 70° from the horizontal, diffraction data comes from a very thin surface layer meaning that the results are very surface sensitive. During

scans, an acceleration voltage of 20 kV and aperture size of 50 µm were used. The size of the scan region was determined according to the grain and substructure size as either 60µmx90µm or 240µmx320µm. The step size showing the scan rate of the selected region was kept at 150 nm for all scans. Samples for EBSD scans were prepared to obtain a perfectly clean surface. Standard metallographic techniques followed by jet electropolishing using a solution of perchloric acid (5%) and methanol at -40°C with an applied voltage of 20 V were used for this purpose.

Neutrons are a proven tool to characterize materials, in particular nuclear materials [39]. Bulk texture measurements probing the grain orientation distribution function over the complete volume of each sample were collected on the HIPPO instrument at the pulsed neutron spallation source at LANSCE [40]. HIPPO is a general purpose TOF diffractometer described in detail by Wenk et al. [41] and only a brief description is given here. The sample is located ~9m from the neutron moderator and diffracted neutrons are detected by 1240 $^{3}$He tubes arranged on panels distributed over five conical rings with scattering angles ranging from 2θ=40° to 150°. A large sample chamber can accommodate ancillary equipment such as an automatic sample changer, furnaces, cryo-equipment, a load frame, high pressure cells or a magnet. For this measurement, samples were glued on standard HIPPO sample holders and loaded into the robotic samples changer [42]. Samples were rotated around the vertical axis and data was collected at 0, 67.5 and 90 degrees for ~20 minutes per orientation. The data was analyzed by simultaneous Rietveld analysis of 15 diffraction patterns with the E-WIMV representation with a 10 degree resolution of the orientation distribution function. Details for the data analysis for texture measurements can be found in Ref [43]. Whole tubes having a height ~10 mm have been used for the neutron diffraction experiments.

**Results:**

***Tube Processing by Process I (HVOF + Hydrostatic Extrusion):***

Process I results in the microstructures where the effect of pure hydrostatic extrusion can be observed. Figure 4.a shows the orientation distribution of the grains in the 14YWT sample produced by Process I which was obtained by the OIM (orientation imaging microscopy) analysis. The coordinates of the map rotated in such a way that the extrusion direction is in through page direction. Consequently, predominantly existing green color infers that most of the grains are oriented with (110) plane normal parallel to the sample extrusion direction. Figure 4.b shows the image quality map of the microstructure which has quite homogenous grain size distribution. Grain size distribution plot in Figure 4.c gives an average grain size of ~2µm. Figure 4.d shows that thermal spraying followed by hydrostatic extrusion results in large number of low angle grain boundaries (~53%) having misorientation angle of $2^{\circ}<\theta<15^{\circ}$.

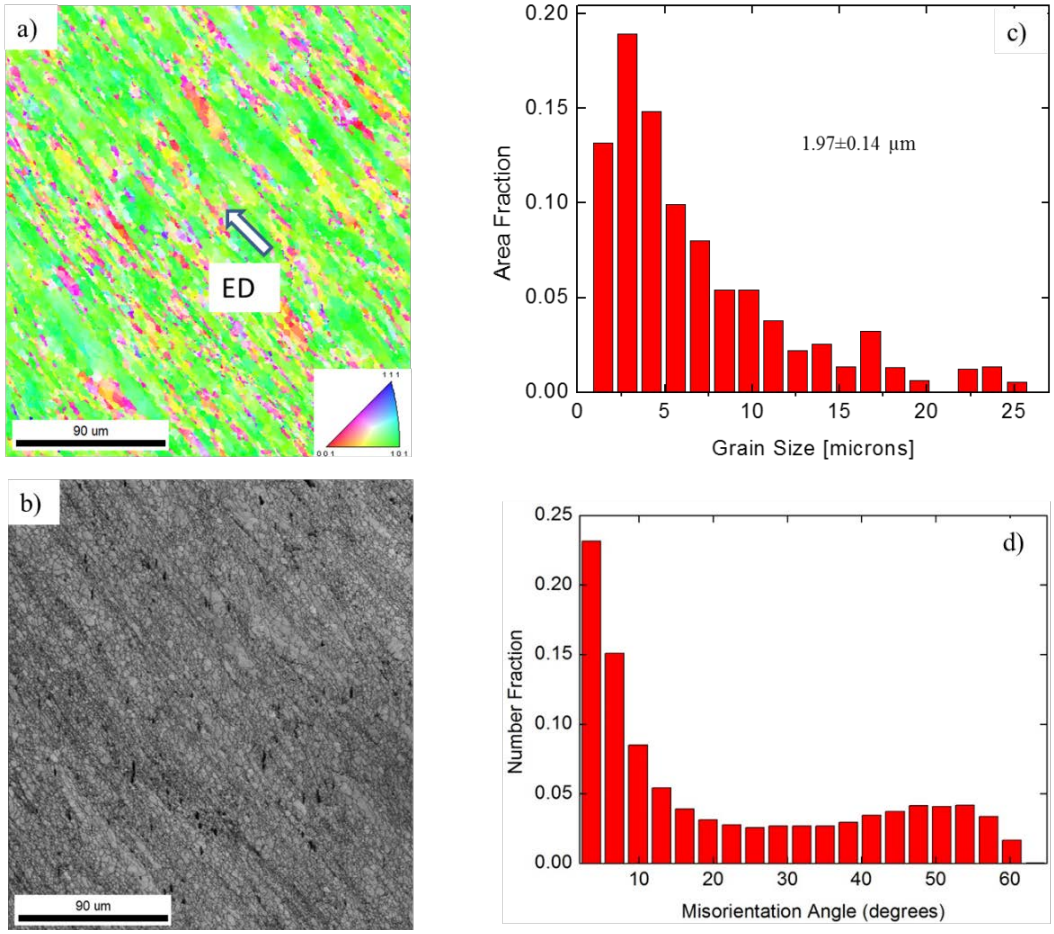


Figure 4. a) Orientation map showing the crystallographic orientation of grains b) grain size distribution as a function of area fraction with an average grain size of 1.97±0.14 µm and c) grain boundary misorientation angle distribution indicating ~53% of LABs in 14YWT samples produced by Process I. (ED:extrusion direction)

Figure 5 shows the pole figures of the sample produced by Process I as determined by both neutron diffraction (Fig. 5.a) and EBSD (Fig. 5.b). Even though data processing functions and probed sample volumina are different for neutron diffraction and EBSD, they give almost the same pole figures with a slight difference in the texture indices. From the pole figures it is obvious that hydrostatic extrusion with 44% equivalent strain results in typical fiber texture of <110>//ED. This is a typical α-fiber texture that was commonly reported by several authors in other ferritic alloys [7,44,45].

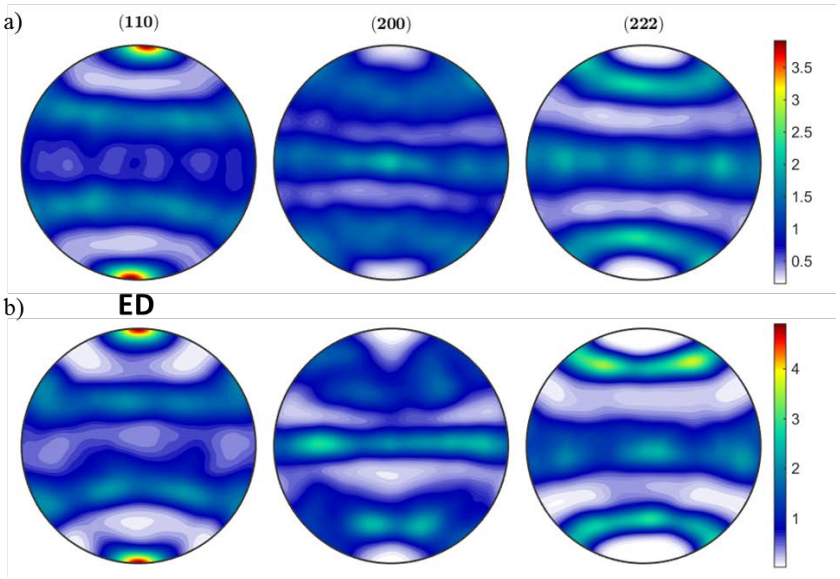


Figure 5: Pole figures of 14YWT samples (process I) obtained by a) Neutron diffraction and b) EBSD techniques. (ED: extrusion direction) Pole figures were processed and plotted with the MTEX package [46].

The ideal orientations of texture components in BCC materials are shown schematically for φ2 = 0˚ and 45˚ ODF sections in Fig. 6 and Table 1. For BCC steels, the important fibers are the α-fiber (<110>∥RD), ε-fiber (<011>∥TD), γ-fiber (<111>∥ND), η-fiber (<100>∥RD), θ-fiber (<001>∥ND), and ζ-fiber (<011>∥ND) [26,27]. It should be noted that 'RD' will be replaced by 'ED' throughout the paper.

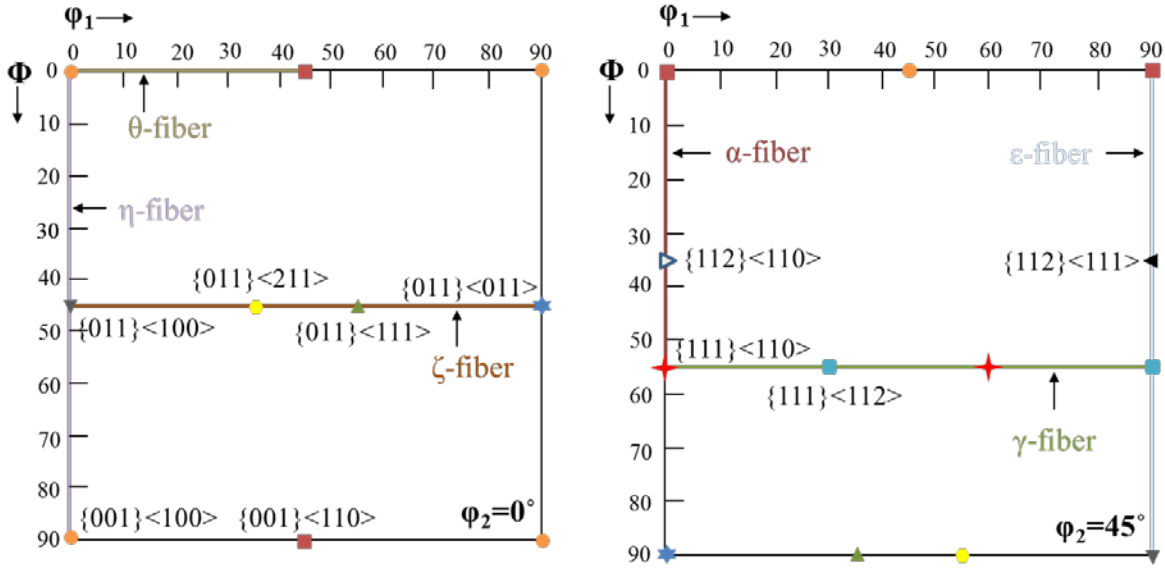


Figure 6: Schematic illustration of the important texture components in BCC materials (*Reproduced from Ref [47]*).

Table 1: Important fibers and orientations for BCC materials [47].

| Fiber name | Fiber axis | Components |
|---|---|---|
| α | <110>∥RD | {001}<110>,{112}<110>, {111}<110> |
| ε | <011>∥TD | {001}<110>, {112}<111>, {111}<112>, {011}<100> |
| γ | <111>∥ND | {111}<110>, {111}<112> |
| η | <100>∥RD | {001}<100>, {011}<100> |
| θ | <001>∥ND | {001}<100>, {001}<110> |
| ζ | <011>∥ND | {011}<100>, {011}<211>, {011}<111>, {011}<011> |

EBSD is a versatile and easy technique to do texture analysis; however, depending on the uniformity of the samples, it might not give very representative results since it can probe only a limited volume on the prepared surface. However, Figure 5 confirms that the probed area using OIM analysis represents the bulk texture obtained by neutron diffraction well. Therefore, we conclude that significant texture gradients are not present in Process I produced tube. Still, to represent the bulk texture, detailed analysis on orientation distribution function (ODF) plots were obtained using the neutron diffraction method. It is worthwhile to point out that while neutron diffraction probes a much larger volume than OIM, all spatial information is lost. Hence, while the detailed texture analyses were employed using neutron diffraction, only OIM can provide grain misorientation angles and orientation maps.

ODF may be represented in Euler space by using Euler angles of $\varphi_1$, $\phi$ and $\varphi_2$. Figure 7 shows the ODF maps of the 14YWT sample produced by Process I at constant $\varphi_2$ values. If $\varphi_2$=0° and $\varphi_2$=45° sections are considered and compared with Figure 6, it can be seen that the texture type is α-fiber at <110> having the strongest intensity on {001}<110>. Furthermore, weak γ-fiber component of {111}<110> and ζ-fiber on {011}<211> and {011}<011> can be observed. The overall texture index was calculated as 2.6 using ODF neutron diffraction data indicating a moderate texture strength knowing that the texture index is 1 for a perfectly random texture and infinite for a single crystal.

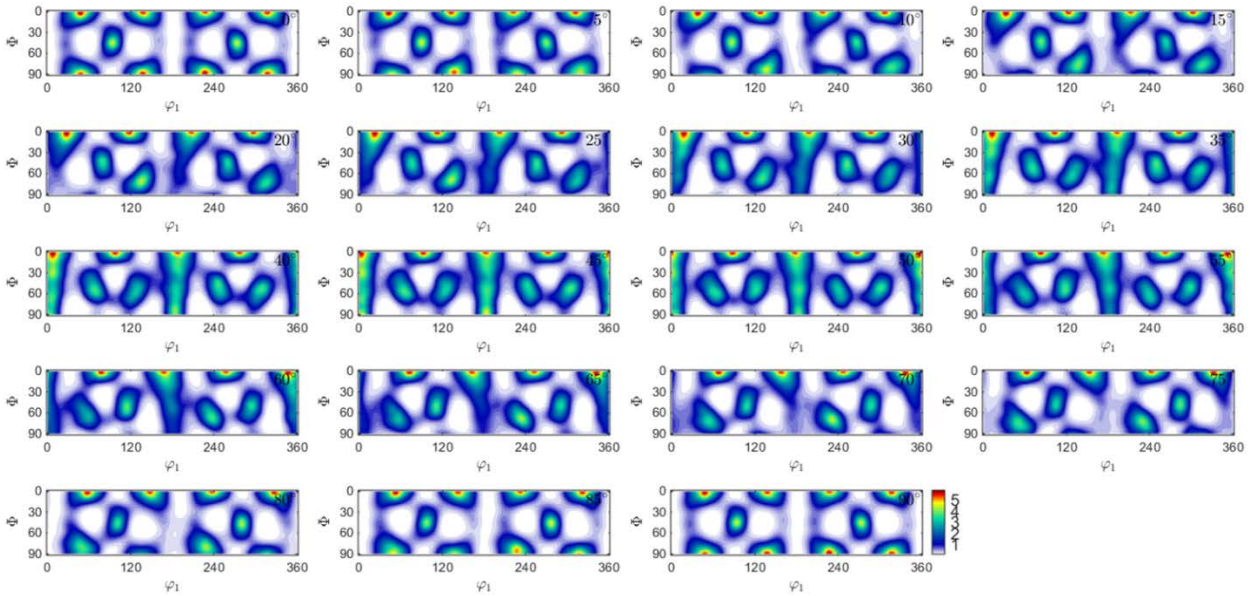

Figure 7: ODF, represented as sections in Euler space, of the 14YWT sample produced by process I at constant $\varphi_2$ values.

***Tube processing by Process II (Rolling +hydrostatic extrusion):***

Figure 8.a shows the orientation distribution of the grains in a 14YWT intermediate tube EDM-cut from a sheet produced by hot extrusion+annealing+hot cross-rolling as described in Figure 2. Since this material was characterized before the final hydrostatic extrusion process, we term this sample the "intermediate tube". The arrows indicate the initial extrusion direction (ED) together with 90° final rolling direction (RD). The coordinates of the map rotated in such a way that the radial direction of the tube (normal direction-ND) is in through page direction. Consequently, predominantly existing red color infers that most of the grains are oriented with (100) plane normal parallel to the sample normal direction. Figure 8.b and 8.c show that the intermediate tube has a bimodal grain size distribution with an average grain size of~ 0.5 μm. Moreover, Figure 8.d shows that the EDM-cut intermediate tube has a much smaller number of low angle grain boundaries (~32%).

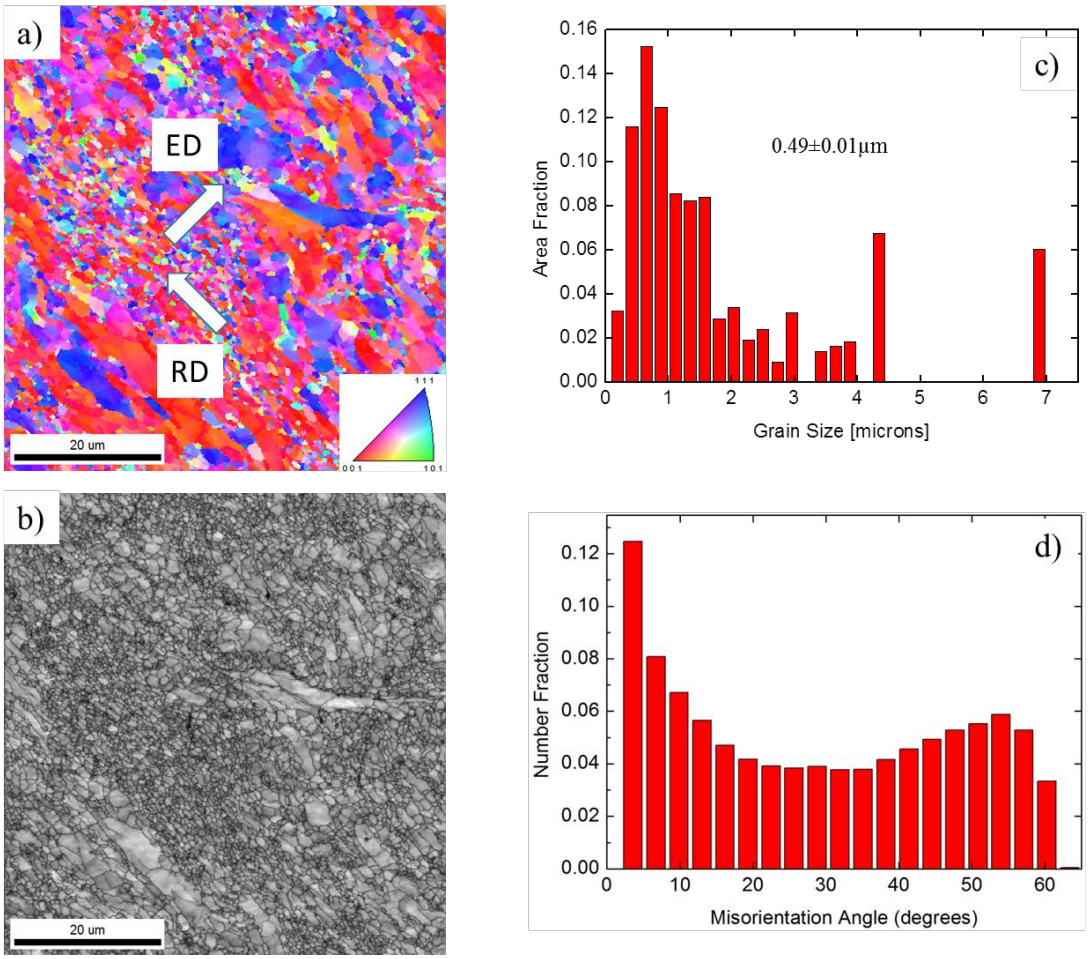


Figure 8: a) Orientation map showing crystallographic distribution of the grains b) band contrast map showing the microstructure in gray scale c) grain size distribution with an average grain size of 0.49±0.01 μm and d) grain boundary misorientation angle distribution indicating ~32% of LABs in intermediate 14YWT tube. (ED:extrusion direction, RD: rolling direction)

Figure 9 shows the pole figures of the intermediate tube determined by both neutron diffraction (Fig. 9.a) and EBSD (Fig. 9.b). Similarity of the pole figures calculated by both methods with slight intensity differences is observed. In order to determine the texture type of materials, their rolling, transverse and normal directions should be assigned correctly. Therefore, it should be determined that either rolling direction or extrusion direction will be the 'transverse direction (TD)'. Since the axial direction of all tubes is in the extrusion direction, in order to be able to use the same coordinate system ED is kept as RD for intermediate tube even though it has a 'real rolling direction'. In other words, final cross-rolling direction was taken as 'TD' and initial extrusion direction was taken as 'RD'. Hence, pole figures indicate that the intermediate tube has texture of both <110>//TD and <200>//ND. The overall texture index was calculated as 10.1 using neutron diffraction, indicating a strong texture.

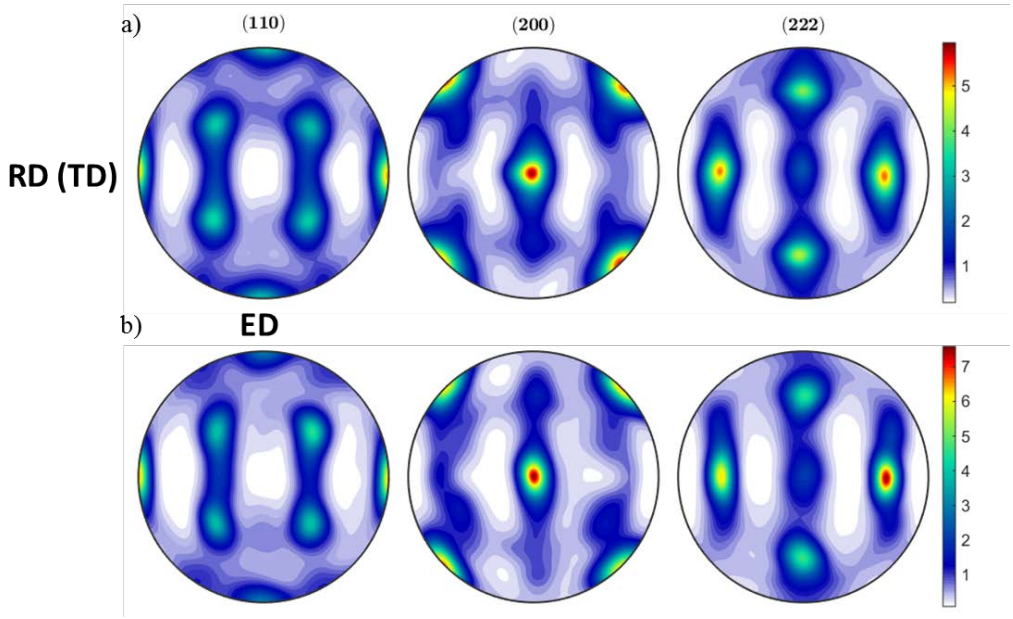


Figure 9: Pole figures of intermediate 14YWT tube obtained by a) Neutron diffraction and b) EBSD techniques.

Figure 10 shows the sections in Euler space of the ODF of the intermediate 14YWT tube at constant $\varphi_2$ values. If $\varphi_2$=0° and $\varphi_2$=45° sections are considered and compared with Figure 6, it can be seen that intermediate tube has strong θ- and ε-fiber on {001}<110> together with a weak γ-fiber on {111}<112>.

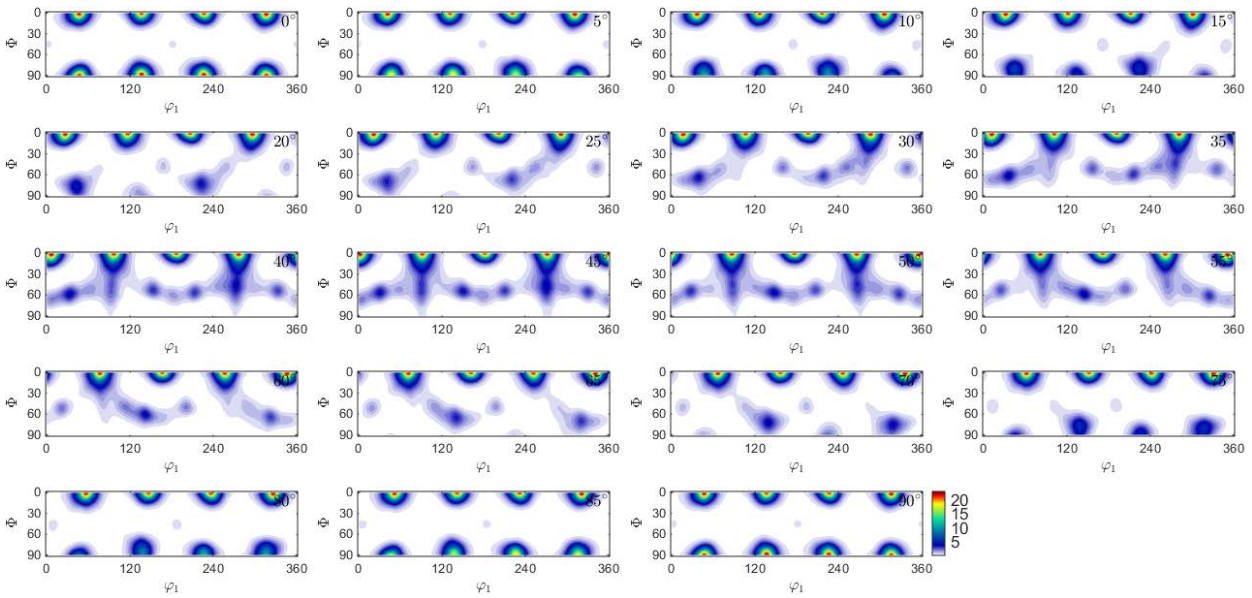


Figure 10: ODF, represented as sections through Euler space, of the intermediate 14YWT tube at constant $\varphi_2$ values.

Figure 11.a shows the orientation map of the grains in 14YWT tube after final hydrostatic extrusion as described in Figure 2. The coordinates of the map rotated in such a way that the

extrusion direction is in through page direction. Consequently, predominantly existing green color infers that most of the grains are oriented with (110) plane normal parallel to the sample extrusion direction. Image quality map in Figure 11.b and 11.c show that very small and larger grains exist which infers a bimodal grain size distribution with an average grain size of ~0.5µm. Figure 11.d shows that after hydrostatic extrusion the amount of low angle grain boundaries increase from 32% to 46%.

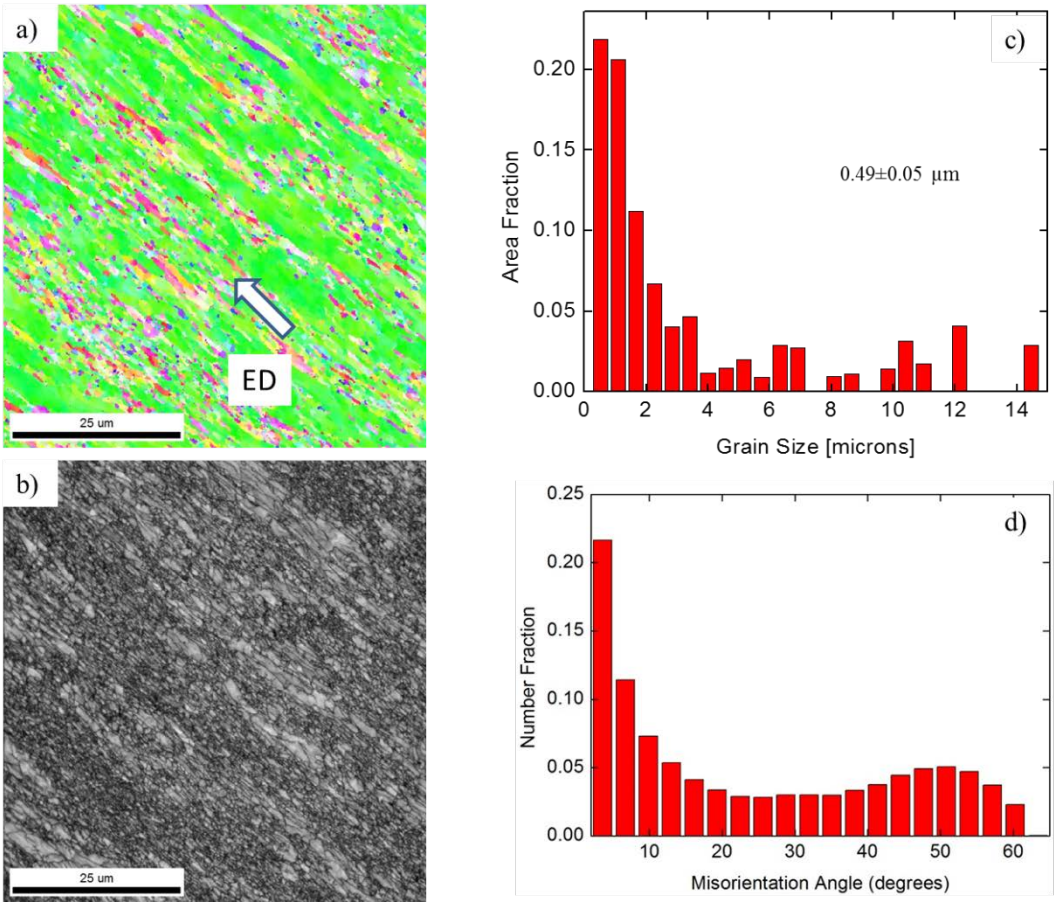


Figure 11: a) Orientation map showing the grains mostly oriented on (101) b) grain size distribution with an average grain size of 0.49±0.05 µm and c) grain boundary misorientation angle distribution indicating ~46% of LABs in 14YWT final tube produced by Process II. (ED:extrusion direction)

Figure 12 shows the pole figures of tube after hydrostatic extrusion derived by both neutron diffraction (Fig. 12.a) and EBSD (Fig. 12.b). It was shown that both methods give not exactly the same results. While the neutron diffraction results in a broken fiber texture <110>//ED, EBSD gives maximum texture index on (200). The difference between the bulk texture (by neutron diffraction) and local texture (by EBSD) infers that the microstructure is not homogenous everywhere. Hence, relying on the neutron diffraction data is better. Neutron diffraction pole figures indicate that the texture is mainly in the extrusion direction. Initial processing steps of hot extrusion+annealing+hot cross-rolling leads the discontinuity in the fiber texture as in Figure 12.a. The overall texture index was calculated as 8.6 using neutron diffraction. The strength of texture decreased from 10.1 to 8.6 after hydrostatic extrusion of intermediate tube with 25% equivalent strain as the hydrostatic extrusion direction is on the opposite direction to the hot

cross-rolling. Consequently, this and Process I indicate that hydrostatic extrusion results in relatively weak textures.

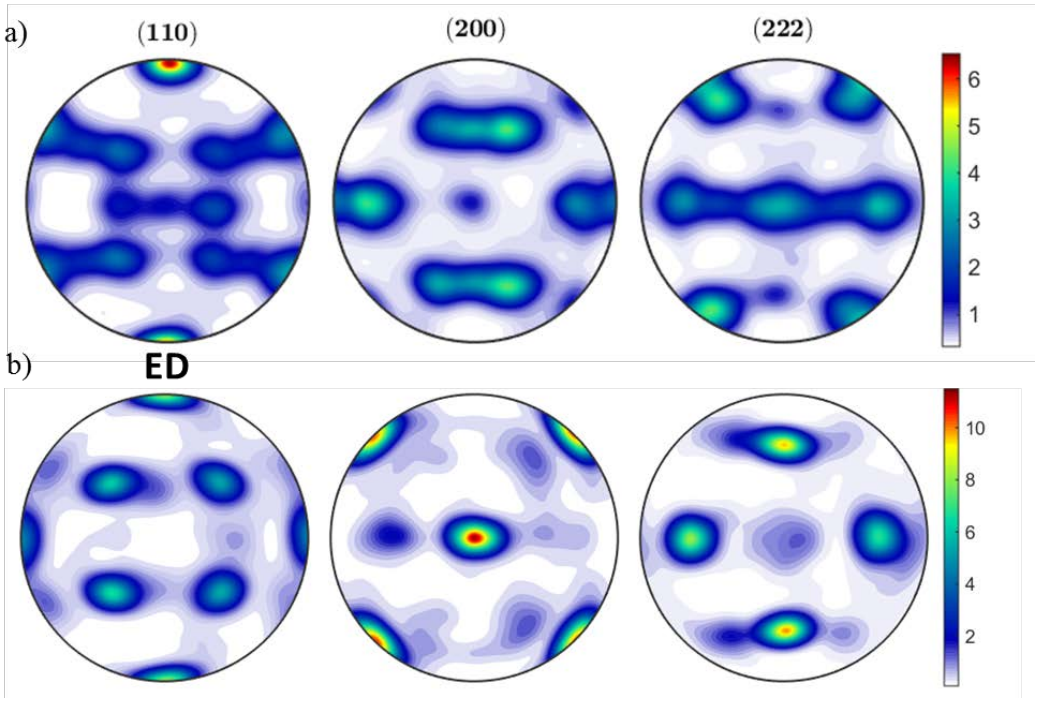


Figure 12: Pole figures of 14YWT final tube after hydrostatic extrusion obtained by a) Neutron diffraction and b) EBSD techniques.

Figure 13 shows the ODF maps of the 14YWT final tube produced by Process II at constant $\varphi_2$ values. Since the poles on (110) were shifted a little bit probably because of the tilt in the tube axis during experiments, $\varphi_2$=50° section gives the maximum texture index. If $\varphi_2$=0° and $\varphi_2$=45° conditions are considered and compared with Figure 6, it can be seen that α-fiber has the maximum intensity on {111}<110>. Besides, final tube has a weak discontinuous γ-fiber on {001}<110>. If $\varphi_2$=0° section is considered in Figure 13, it can be seen that the sample has very weak ζ-fiber texture on {011}<211> and {011}<011>.

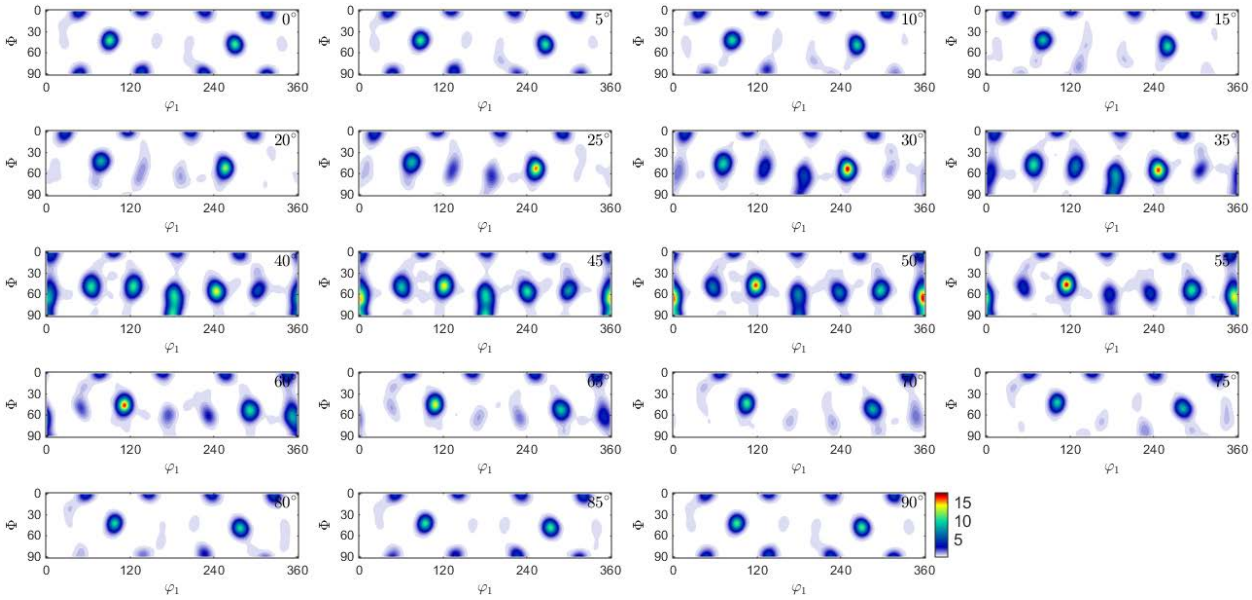


Figure 13: ODF, represented as sections through Euler space, of the 14YWT final tube after hydrostatic extrusion at constant $\varphi_2$ values.

**Discussion:**

Hydrostatic extrusion leads to a strong preferred crystal orientation on <110>//ED. In general, deformation textures in BCC steels are reported to be either α-fiber or γ-fiber or their combination. On the other hand, this study shows that the hydrostatic extrusion causes additional weak ξ-fiber which is a typical shear deformation texture in BCC metals [48]. Consequently, it can be inferred that hydrostatic extrusion is not a total plane strain deformation causing a strong rolling texture. It is rather a combination of plain strain and simple shear resulting in a strong α-fiber and weaker and discontinuous γ- and ξ-fiber.

The texture of the materials deformed by shear was found to be considerably weaker when compared to equivalently strained rolled specimens due to material rotation during simple shear which does not result in stable orientations [49, 50-52]. Similarly, the texture index after 44% equivalent strained hydrostatic extrusion in Process I is quite low, 2.6, compared to the final rolling texture of the intermediate tube in Process II which is 50% equivalent strained (10.1).

Gazder et al. [48] studied the effect of equal-channel angular extrusion (ECAE), a shear process, on the texture in interstitial free BCC steels. It was found that while the initial pass creates a strong J-type{110}<112> shear texture, increasing accumulated strain resulted in the strengthening of E {001}<111> and D {112}<111> type components and the weakening of J-type {110}<112> orientations (see Table 2). From the above findings it can be inferred that amount of extrusion and introduced shear deformation is not enough to create large amount of accumulated strain neither to cause strong J-type shear nor a deviation from the J-type shear texture [48].

Table 2: Ideal orientations of important simple shear texture components observed in the $\varphi 2 = 0^\circ$ and $45^\circ$ sections of orientation distribution functions (ODF) for bcc metals [53]

| Component | Miller indices | Euler angle | | |
|---|---|---|---|---|
| | | φ1 | Φ | φ2 |
| F | $(110)[001]$ | 0, 180, 360, 90,<br>270 | 45<br>90 | 0<br>45 |
| D1 | $(\bar{1}\bar{1}2)[111]$ | -<br>90 | -<br>35 | -<br>45 |
| D2 | $(11\bar{2})[111]$ | -<br>270 | -<br>35 | -<br>45 |
| E1 | $(01\bar{1})[111]$ | 55, 235<br>145, 325 | 45<br>90 | 0<br>45 |
| E2 | $(0\bar{1}1)[111]$ | 125, 305<br>35, 215 | 45<br>90 | 0<br>45 |
| J1 | $(0\bar{1}1)[\bar{2}11]$ | 35, 215<br>125, 305 | 45<br>90 | 0<br>45 |
| J2 | $(1\bar{1}0)[\bar{1}\bar{1}2]$ | 145,325<br>55, 235 | 45<br>90 | 0<br>45 |

Similarly, the presence of a large amount of low-angle grain boundaries indicates that the material can even accumulate more strain [54], allowing application of further deformation [55]. After low angle grain boundaries reach to high enough strains that cannot be stored, recrystallization occurs leading to strain free grains with high angle grain boundaries. Figure 14 indicates that hydrostatic extrusion used for both Process I and Process II results in large amount of low angle grain boundaries compared to the intermediate tube before hydrostatic extrusion in Process II. This means that even two passes of hydrostatic extrusion in Process I is not enough to create necessary strain to form a whole microstructure consisting of recrystallized grains which is the indication of incomplete dynamic recrystallization.

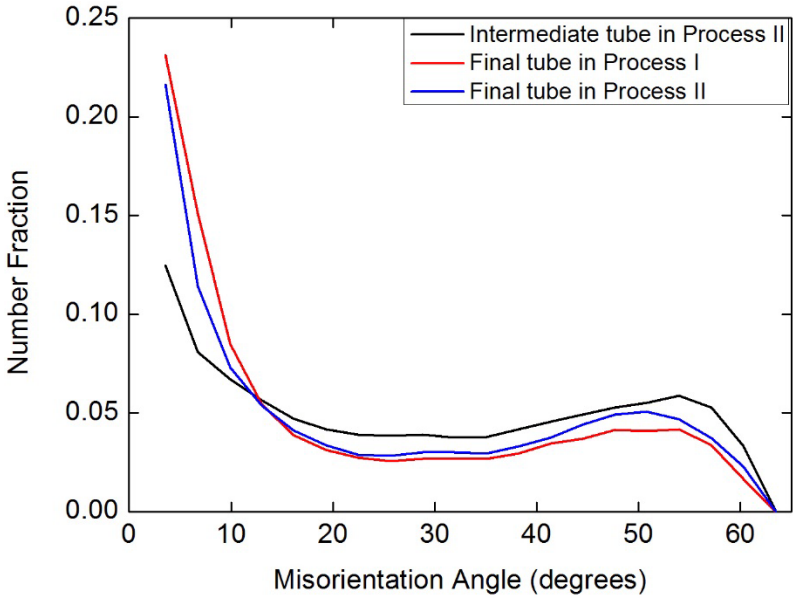


Figure 14: Grain boundary misorientation angle distribution of three different tubes produced by Process I&II.

The stored energy at the grain boundaries can be investigated by Kernel average misorientation distribution maps as shown in Figure 15. Hydrostatically extruded final tubes in Figure 15.a and 15.c show that average misorientation degree is much higher mostly at the low angle grain boundaries which are shown in black color. On the other hand, the intermediate tube (Figure 15.b) which was exposed to hot extrusion, annealing and final cross-rolling steps has much lower stored energy at the grain boundaries because of strain relief as a result of recrystallization.

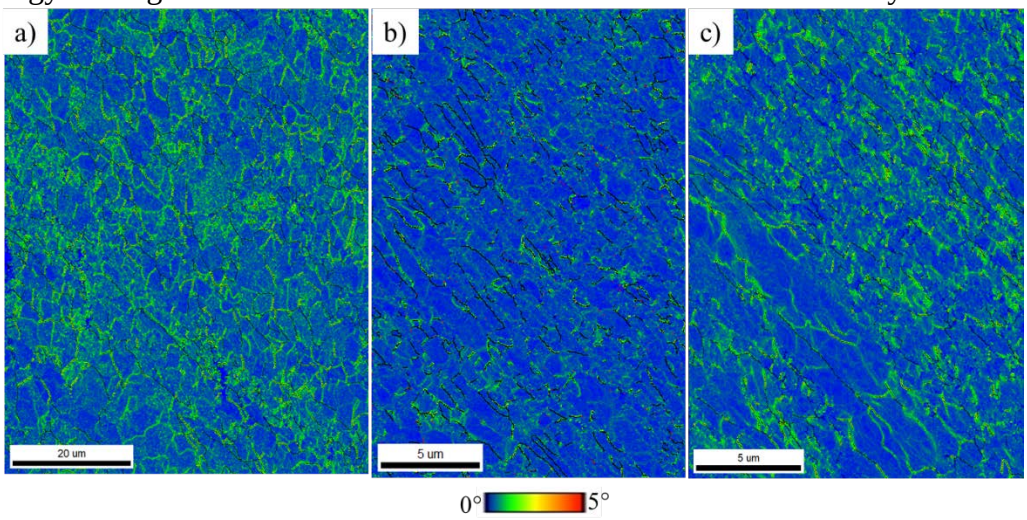


Figure 15: Kernel average misorientation maps of 14YWT a) final tube produced by Process I b) intermediate tube produced by Process II and c) final tube produced by Process II (low angle grain boundaries were shown in black).

The boundary type distribution has been shown in Figure 16. For all cases, the amount of coincidence site lattice (CSL) boundaries which are special boundaries giving the materials improved properties are less than 10%. Hydrostatic extrusion increases the amount of LABs

because of the incomplete dynamic recrystallization. On the other hand, intermediate tube has the lowest amount of LABs and highest amount of random HABs indicating higher amount of recrystallization.

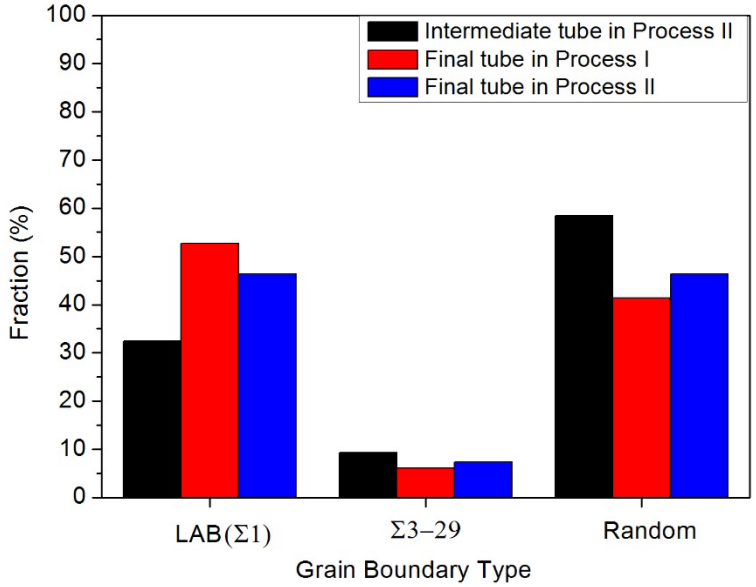


Figure 16: Grain boundary types and their fraction as a result of different processing methods.

**Conclusions:**

In this study, the effect of the different processing routes for fabrication of tubes from 14YWT NFAs on the texture and grain boundary characteristics have been investigated. It was found that hydrostatic extrusion up to 44% of equivalent strain results in combination of rolling and shear textures, former being much pronounced. In other words, strong α and weak γ fibers occur on {001}<110> and {111}<110> while very weak ζ-fiber occurs on {011}<211> and {011}<011>. The overall texture of the sample produced by Process I is quite low, 2.6, after 44% of deformation. On the other hand, the intermediate tube produced through hot extrusion+annealing+cross-rolling shows strong rolling textures of θ- and ε-fiber on {001}<110> together with weak γ-fiber on {111}<112>. Even though the equivalent strain (~ 50% ) introduced during hot cross-rolling is very close to the one introduced during hydrostatic extrusion in Process I, the overall texture index after hot rolling is 10.1. After hydrostatic extrusion of the intermediate sample in the perpendicular direction of hot cross-rolling, the texture type changes into α, γ and ζ-fibers. Together with this, shear deformation with 25% equivalent strain introduced during hydrostatic extrusion in Process II decreases the overall texture index to 8.6. When the grain boundary characteristics are considered, hydrostatic extrusion up to equivalent strain of 44% results in large number of low angle grain boundaries. This shows that the total stored energy at the grain boundaries is not enough for the recrystallization and further extrusion steps are possible. On the other hand, as a result of the intermediate tube processing routes, the amount of high angle grain boundaries is high showing that this processing route introduces enough deformation required for the recrystallization.

**References:**

[1] D.A. McClintock, D.T. Hoelzer, M.A. Sokolov, R.K. Nanstad, J. Nucl. Mater. (386– 388) (2009) 307–311.

[2] S.M. Ukai, M.Fujiwara, J. Nucl. Mater. (307–311) (2002) 749–757.

[3] R. Lindau, A. Moslang, M. Rieth, M. Klimiankou, E. Materna-Morris, A. Alamo, A.-A.F. Tavassoli, C. Cayron, A.-M. Lancha, P. Fernandez, N. Baluc, R. Schaublin, E. Diegele, G. Filacchioni, J.W. Rensman, B. v.d.Schaaf, E. Lucon, W. Dietz., Fusion Eng. Des. (75–79) (2005) 989–996.
[4] D.T. Hoelzer, J. Bentley, M.A. Sokolov, M.K. Miller, G.R. Odette, M.J. Alinger, J. Nucl. Mater. (367–370) (2007) 166–172.
[5] Abd El-Azim, M.E., Mechanics of Materials 25 (1997) 255–261.
[6] Klueh, R.L., Alexander, D.J., J. of Nucl. Mater. 233–237 (1996) 336–341.
[7] Z. Oksiuta, P. Hosemann, S.C. Vogel, N. Baluc, J. of Nucl. Mater. 451 (2014) 320–327.
[8] G.R. Odette, M.J. Alinger and B.D. Wirth, Ann. Rev. Mater. Res. 38 (2008) 471.
[9] G.R. Odette and D.T. Hoelzer, JOM J. Minerals Metals Mater. Soc. 62 (2010) 84.
[10] T. Yamamoto, G.R. Odette, P. Miao, D.J. Edwards and R.J. Kurtz, J. Nucl. Mater. 386–388 (2009) 338.
[11] G.R. Odette, P. Miao and D.J. Edwards, J. Nucl. Mater. 417 (2011) 1001.
[12] Hayashi, T., Sarosi, P.M., Schneibel, J.H., Mills, M.J., Acta Mater. 56 (2008) 1407–1416.
[13] Z. Oksiuta, M. Lewandowska, K.J. Kurzydłowski, Mechanics of Materials 67 (2013) 15–24.
[14] S. Ukai, M. Fujiwara, J. Nucl. Mater. 307–311 (2002) 749–757.
[15] D.T. Hoelzer, J. Bentley, M.A. Sokolov, M.K. Miller, G.R. Odette, M.J. Alinger, J. Nucl. Mater. 367–370 (2007) 166–172.
[16] T.S. Byun, J.H. Kim, D.T. Hoelzer, J. Nucl. Mater. 407 (2010) 143–150.
[17] T.S. Byun, J.H. Kim, J.H. Yoon, D.T. Hoelzer, J. Nucl. Mater. 407 (2010) 78–82.
[18] S. Zherebtsov, A. Mazur, G.Salishchev, W. Lojkowski, Mater. Sci. Eng. A 485 (2008) 39–45.
[19] S. Zherebtsov, G.Salishchev, W. Lojkowski, Mater. Sci. Eng. A 515 (2009) 43–48.
[20] M. Lewandowska, A.T. Krawczynska, M. Kulczyk, K.J. Kurzydłowski, J. Nucl. Mater. 389-388 (2009) 499–502.
[21] J.J. Lewandowksi, B. Berger, J.D. Rigney, S.N. Patankar, Phil. Mag. 78(3) (1998) 643-656.
[22] R.W. Margevicius, J.J. Lewandowski, I.E. Locci, *Scripta metall. mater.* **29 (**1992) 1733.
[23] R.W. Margevicius, J.J. Lewandowski, *Scripta metall.* 2017(25) (1991) 1993a
[24] R.W. Margevicius, J.J. Lewandowski, I.E. Locci, R.D. Noebe, *Scripta metall. mater.* 29 (1993) 1309.
[25] YS Liu, L Delannay, P. Van Houtte, Acta Matter. 50 (2001) 1849.
[26] F.J. Humphreys and M. Hatherly, Recrystallization and Related Annealing Phenomena, 2nd ed., Elsevier Science Ltd., Oxford, UK, 2004.
[27] O. Engler and V. Randle, Introduction to Texture Analysis—Macrotexture, Microtexture, and Orienatation Mapping, 2nd ed., Taylor & Francis Group, New York, 2010.
[28] J. Asensio, G. Romano, Mater Characterization 47 (2001) 119.
[29] CL Xie, E. Nakamachi, Mater Sci Eng A 340 (2003) 130.
[30] WB. Hutchinson, Int Met rev 29 (1984) 25.
[31] RK. Ray, JJ. Jonas, RE. Hook, Int Mat Rev 39 (1994) 129.
[32] WT Read, W. Shockley, Phys Rev 78 (1950) 275.
[33] I Samajdar, B Verlinden, P Van Houtte, D. Vanderschueren, Mater Sci Eng A 238 (1997) 343.
[34] FJ. Humphreys J Mater Sci 36 (2001) 3833.
[35] S-H Choi, Y-S. Jin, Mater Sci Eng A 371 (2004) 149.
[36] J.-Y. Kang, B. Bacroix, H. Regle, K.H. Oh, H.-C. Lee, Acta Mater. 55 (2007) 4935–4946.

[36] N. J. Cunningham, Y. Wu, G. R. Odette, D. Gragg, K. Fields, D. T. Hoelzer, and S.A. Maloy, "Characterization of the Final Precursor Alloy to a Larger Best Practice Heat of 14YWT," DOE Fusion Reactor Materials Program Semiannual Progress Report for the Period Ending December 31, 2012, DOE/ER-0313/53.
[37] B.L. Adams, Ultramicroscopy 67 (1997) 11-17.
[38] V. Kumar, IEEE Transactions on Image Processing, 22 (7) (2013) 2637-2645.
[39] S.C. Vogel, ISRN Materials Science, 2013 (2013) 1-24.
[40] P.W. Lisowski, K. F. Schoenberg, *Nuclear Instruments and Methods in Physics Research A* 562 (2) (2006) 910–914.
[41] H.R. Wenk, L. Lutterotti, S.C. Vogel, Nuclear Instruments and Methods in Physics Research A 515 (2003) 575–588.
[42] A.S. Losko, S.C. Vogel, H.M. Reiche,H. Nakotte, J. Appl. Cryst. 47 (2014) 2109–2112.
[43] H.R. Wenk, L. Lutterotti, S.C. Vogel, Powder Diffraction 25 (3) (2010) 283-296.
[44] D. Orlov, P.P. Bhattacharjee, Y. Takada, M. Umemoto, N. Tsuji, Scr. Mater. 60 (2009) 893896.
[45] R. Kasada, S.G. Lee, J. Isselin, J.H. Lee, T. Omura, A. Kimura, T. Okuda, M. Inoue, S. Ukai, S. Ohnuki, T. Fujisawa, F. Abe, J. Nucl. Mater. 417 (2011) 180–184.
[46] R. Hielscher, H. Schaeben, J. Appl. Cryst. (2008). 41, 1024–1037.
[47] R. Jamaati, M.R. Toroghinejad, M.A. Mohtadi-Bonab, H. Edris, J.A. Szpunar, M.R Salmani, JMEPEG 23 (2014) 4436–4445.
[48] A.A. Gazder, F. Dalla Torre, C.F. Gu, C.H.J. Davies, E.V. Pereloma, Mater Sci Eng A 415 (2006) 126–139.
[49] W.H. Huang, L. Chang, P.W. Kao, C.P. Chang, Mater. Sci. Eng. A 307 (2001) 113.
[50] U.F. Kocks, C.N. Tome, H.-R. Wenk, Texture and Anisotropy: Preferred Orientations in Polycrystals and Their Effect on Material Properties, first ed., Cambridge University Press, Cambridge, 1998.
[51] S.R. Agnew, J.R. Weertman, Mater. Sci. Eng. A 244 (1998) 145.
[52] J.R. Bowen, The Formation of Ultra-fine Grained Model Aluminium and Steel Alloys, Ph.D. Thesis, UMIST, 2000.
[53] M.R. Barnett, M.D. Nave, K. Chu, A. Oudin, in: IMEA Ltd. (Ed.), Proceedings of the Second International Symposium on Ultrafine Grained Structures (ISUGS), Geelong, Australia, 2003, CDROM.
[54] Y. Estrin, A. Vinogradov, Acta Mater., 61 (2013) 782–817.
[55] K. Ozaltin, W. Chrominski, M. Kulczyk, A. Panigrahi, J. Horky, M. Zehetbauer, M. Lewandowska, J Mater Sci 49 (2014) 6930–6936.